June 26-30, 2023, Boston, Massachusetts

GT2023-100921

INTEGRATED CONTROL DESIGN FOR A PARTIALLY TURBOELECTRIC AIRCRAFT PROPULSION SYSTEM

Donald L. Simon NASA Glenn Research Center Cleveland, OH, USA Santino J. Bianco NASA Glenn Research Center Cleveland, OH, USA Marcus A. Horning HX5, LLC Brook Park, OH, USA

ABSTRACT

Electrified Aircraft Propulsion (EAF for reducing aviation emissions and fuel architectures have been proposed turboelectric configurations that combine motor-driven propulsors. Such architect between subsystems and thus require solution. To address this need, this paper control design strategy for a commercial turboelectric aircraft concept consisting turbofan engines and an electric motor di Within this architecture the turbofans ser generating thrust and supplying mechani to generate electricity for the tailfan n control system is tasked with coordinatin operation under both steady-state and tr paper introduces a linear state-space architecture reflecting the coupling bety tailfan subsystems along with loop transf open- and closed-loop system dynamics. applied strategy for scheduling the tail; based on the average sensed fan speed of approach ensures synchronized operatio tailfan subsystems while also allowing th design to be simplified. Performance of design is assessed through a real-time had conducted at the NASA Electric Aircraft To a scaled version of the electrical system shaft dynamics were implemented in hardware and evaluated under closed-loo this facility test are presented to illustr applied integrated control design approa and transient scenarios including a full-fa

Keywords: Electrified Aircraft Propulsion, Aircraft Propulsion Controls, Integrated Control Design

NOMENCLATURE					
P) holds great potential	Acronyms				
l burn. A variety of EAP	BLI	Boundary layer ingestion			
including partially-	CLTF	Closed-loop transfer function			
ne turbofan engines with	DC	Direct current			
ctures exhibit coupling	EAP	Electrified aircraft propulsion			
an integrated control	HIL	Hardware-in-the-loop			
er presents an integrated	hp	Horsepower			
al single-aisle partially-	HPC	High pressure compressor			
g of two wing-mounted	LP	Low pressure			
driven tailfan propulsor.	LPC	Low pressure compressor			
erve the dual purpose of	NEAT	NASA electric aircraft testbed			
iical offtake power used	NPSS	Numerical propulsion system simulation			
motor. The propulsion	OLTF	Open-loop transfer function			
ing turbofan and tailfan	PI	Proportional plus integral			
transient scenarios. The	PLA	Power lever angle			
representation of the	rpm	Revolutions per minute			
tween the turbofan and	SISO	Single-input single-output			
sfer functions reflecting	SMICS	Sliding model impedance controller with			
es. Also discussed is an		scaling			
ilfan setpoint command	STARC-ABL	Single-aisle turboelectric aircraft with aft			
f the two turbofans. This		boundary layer propulsion			
ion of the turbofan and	TEEM	Turbine electrified energy management			
the turbofan fuel control	T-MATS	Toolbox for the modeling and analysis of			
f the integrated control		thermodynamic systems			
ardware-in-the-loop test	VAFN	Variable area fan nozzle			
Testbed. During this test	VBV	Variable bleed valve			
em and turbomachinery	VSVs	Variable stator vanes			
in electrical machine					
oop control. Results from	Parameters				
rate the efficacy of the	A, B, C	State space matrices			
oach under steady-state	e(s)	Turbofan closed-loop control error signal			
flight mission profile.	$e_t(s)$	Tailfan closed-loop control error signal			
Propulsion, Aircraft	F(s)	Fuel actuator transfer function			

Tailfan transfer function

This material is declared a work of the U.S. Government and is not subject to copyright protection in the United States. Approved for public release; distribution is unlimited.

 $G_t(s)$

K(s)	Turbofan fuel control transfer function
K_e	Turbofan transfer function gain
K_i, K_p	Fuel control integral and proportional gains
$K_{m,i}, K_{m,p}$	Motor control integral and proportional gains
$K_m(s)$	Tailfan motor control transfer function
K_t	Tailfan transfer function gain
N_{1c}	Corrected turbofan fan speed
\dot{N}_{1c}	Corrected turbofan fan speed derivative
N_{tc}	Corrected tailfan speed
N_{2c}	Corrected turbofan low pressure shaft speed
\dot{N}_{2c}	Corrected turbofan low pressure shaft speed
	derivative
N_{3c}	Corrected turbofan core speed
\dot{N}_{3c}	Corrected turbofan core speed derivative
P_{s3}	Turbofan HPC exit static pressure
Q_m	Tailfan motor torque
r_1, r_2	Turbofan transfer function poles
r_t	Tailfan transfer function pole
S	Laplace operator
T(s)	Tailfan torque transfer function
u,x,y	State space input, state, and output vectors
W_f	Fuel flow
z_I	Turbofan transfer function zero
z_t	Tailfan transfer function zero
γ	Ratio of tailfan to turbofan speed variation

1. INTRODUCTION

Electrified Aircraft Propulsion (EAP) relies on the generation, storage, transmission, and consumption of electrical power to produce aircraft thrust. It expands the design space enabling development of ground-breaking aircraft and propulsion concepts offering a potential step-change reduction in aviation emissions and fuel-burn [1,2,3]. A multitude of EAP concepts have been proposed or are in development including all-electric designs [4], turboelectric designs that combine fuelburning engines and electric motors [5], and hybrid designs that combine fuel-burning engines with electric motors and energy storage devices [6]. The NASA Aeronautics Research Mission Directorate strategic implementation plan outlines a vision for transitioning to alternative propulsion and energy sources, including electrified propulsion [7]. EAP is also a key element of the United States Sustainable Flight National Partnership [8] and Aviation Climate Action Plan [9].

Multiple technology challenges must be addressed to bring EAP to fruition. This includes the development of high efficiency, light weight, flight quality motors, power electronics, and energy storage devices [10], advancements for the safe and reliable transfer of electricity at high power levels at altitude [11], and solutions to address the thermal management challenges associated with EAP [12]. Additionally, EAP introduces new challenges and opportunities from a control perspective [13]. Control of gas turbine engines, which are the conventional non-electrified propulsion systems for commercial transport aircraft, is largely a single-input, single-output (SISO) control problem. Fuel flow serves as the primary input and a

sensed output representative of thrust such as fan speed or engine pressure ratio serves as the feedback parameter. EAP architectures that include fuel-burning engines often present multivariable controls problems with both engine fuel flow and electric machine torque commands serving as inputs, and speeds of the engine and motor driven propulsors serving as outputs. This raises the need for a system-level approach towards control design [14]. Example system-level control strategies that have been proposed for hybrid EAP systems include Turbine Electrified Energy Management (TEEM), which seeks to improve gas turbine engine operability [15], and optimal energy management control strategies to reduce overall fuel consumption [16,17,18].

This paper presents an integrated control design strategy for partially-turboelectric EAP designs consisting of turbofan engines and motor-driven propulsors [2]. Past publications on partially-turboelectric EAP controls include the NASA-authored publications contained in Refs. [19,20,21]. Those publications, as well as this paper, focus on control design for the Single-aisle Turboelectric AiRCraft with Aft Boundary Layer propulsor (STARC-ABL) propulsion system [22,23]. The STARC-ABL is a commercial single-aisle partially-turboelectric concept aircraft proposed by NASA. Its propulsion system consists of two wingmounted turbofan engines and a motor-driven tailfan propulsor. Past NASA STARC-ABL propulsion control design efforts took the approach of either designing separate closed-loop controllers for the turbofan and tailfan subsystems in a decentralized fashion [19,20] or operating the tailfan under open-loop control [21]. Both approaches have their limitations. The decentralized control approach requires a tedious design effort and is prone to operability concerns during rapid transients while the open-loop control approach sacrifices the ability to tightly control tailfan thrust output. To address these shortcomings, the approach presented in this paper develops and applies an integrated control strategy that directly accounts for the coupling between the STARC-ABL's turbofan and tailfan subsystems. This approach promotes operability, enables tighter control of thrust, and simplifies the overall control design effort.

The remainder of this paper is organized as follows. Section 2 provides an overview of the STARC-ABL architecture considered in this study. The integrated control design approach developed for the STARC-ABL is presented in Section 3. This includes the control strategy for coordinating STARC-ABL subsystem operation under both steady-state and transient scenarios. Section 4 presents results from a real-time hardware-in-the-loop (HIL) test of the control design which included a subscale representation of the STARC-ABL's electrical system and simulated turbomachinery elements. Finally, a discussion is presented in Section 5 followed by conclusions in Section 6.

2. STARC-ABL OVERVIEW

Artistic renderings of the STARC-ABL aircraft are provided in Fig. 1. The two wing-mounted turbofan engines serve the dual-purpose of producing thrust and supplying mechanical offtake power that is converted to electricity. The electricity is then delivered to a motor-driven tailfan propulsor that utilizes

boundary layer ingestion (BLI). The STARC-ABL is predicted to provide a 3.4% reduction in fuel burn relative to an advanced technology conventional aircraft for a single-aisle class, 3,500 nautical mile design mission and a 2.7% reduction for a 900 nautical mile economic mission [23].

A block diagram of the STARC-ABL propulsion system is shown in Fig. 2. The engines are geared turbofan designs with an electrical generator attached to the low-pressure (LP) shaft of each engine. Alternating current electrical power produced by each generator is converted to direct current (DC) electrical power by inverters and supplied to a 700V DC bus. Attached to the same DC bus is an inverter that drives a 3500 horsepower (hp) motor attached to the BLI tailfan. System inputs include fuel flow supplied to the turbofans and torque commands supplied to the inverters. Additionally, each turbofan is equipped with a variable bleed valve (VBV) and a variable area fan nozzle (VAFN). The tailfan is also equipped with a VAFN actuator.



Figure 1: STARC-ABL AIRCRAFT

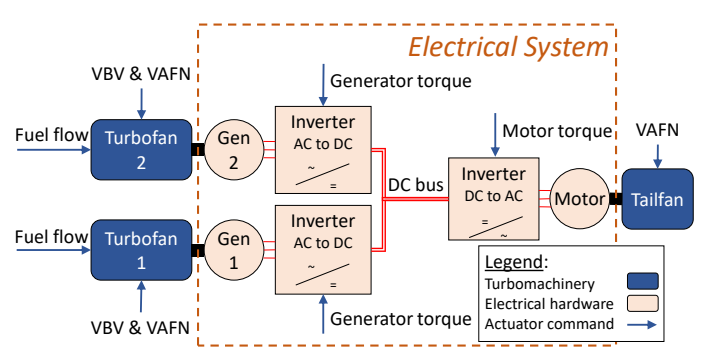


Figure 2: DIAGRAM OF STARC-ABL PROPULSION SYSTEM

3. INTEGRATED CONTROL DESIGN

References [22,23] on the STARC-ABL are primarily system studies focused on steady-state performance and do not specify a control concept of operations for coordinating subsystem operation during transients. For the purposes of developing the control design presented in this paper it is assumed that the tailfan motor draws power from the DC bus to achieve a commanded operating speed while the two generators attached to the turbofans act as bus voltage regulators working to hold a constant 700V level on the DC bus. This results in an "aft-to-forward" coupling in the architecture where changes in tailfan power demand will result in a corresponding change in the amount of power extracted from the turbofans.

The remainder of this section presents the step-by-step process applied for developing a STARC-ABL integrated control design. Section 3.1 discusses development of a nonlinear model used for overall control design and evaluation purposes.

Section 3.2 presents the steady-state scheduling of VBV and VAFN actuator positions and subsystem thrust output. Section 3.3 introduces the integrated control technique applied to promote coordinated turbofan and tailfan operation during transients. Section 3.4 discusses setpoint control design and Section 3.5 covers the acceleration and deceleration control schedules and limit logic. Finally, overall control integration and mode selection logic is presented in Section 3.6.

3.1 STARC-ABL Propulsion System Model

The propulsion system model used in this study is derived from a nonlinear steady-state model of the STARC-ABL coded in the Numerical Propulsion System Simulation (NPSS) environment [24]. The NPSS model is converted to the MATLAB® Simulink® (MathWorks, Natick, MA) environment using the NASA-developed Toolbox for the Modeling and Analysis of Thermodynamic Systems (T-MATS) [25] and a power flow modeling approach [26]. T-MATS is used to model the turbomachinery components; while the power flow modeling approach is used to model electrical system components at turbomachinery time-scales. Shaft dynamics and a transient solver are also included to enable simulation of transient operation. The resulting STARC-ABL T-MATS model is used for full-flight envelope control design evaluation and supports the generation of linear state-space models for control design purposes.

3.2 Steady-State VBV, VAFN, and Thrust Schedules

Variable geometry control actuators included in the STARC-ABL NPSS and T-MATS models are limited to VBV and VAFN actuators. These models do not include turbofan variable stator vane (VSVs) as the "on-schedule" operation of VSVs are reflected in the models' high-pressure compressor (HPC) module. Steady-state schedules of the VBV and VAFN actuator position and subsystem thrust are defined consistent with the original STARC-ABL NPSS model. Each of these schedules are structured as three-dimensional interpolation grids spanning the STARC-ABL flight envelope. The VBV and VAFN schedules are based on altitude, Mach, and corrected fan speed while thrust lookup is based on altitude, Mach, and the power lever angle (PLA) throttle input.

3.2.1 VBV Schedule. Each turbofan engine is equipped with a VBV actuator installed between its low-pressure compressor (LPC) and HPC. The engine control adjusts the VBV open or closed to maintain LPC stall margin. This control adjustment follows an open-loop schedule based on turbofan corrected fan speed (N_{1c}). At low N_{1c} operating conditions the VBV is opened according to a defined schedule that will maintain LPC stall margin at 10% during steady-state operation. At increased N_{1c} speeds the VBV remains fully closed and LPC stall margin will be greater than 10%.

3.2.2 VAFN Schedule. The VAFN actuators are installed in the bypass stream of the STARC-ABL's turbofans and aft of the tailfan's fan module. Control adjustment of these actuators ensures that the fan modules of the respective subsystems follow a steady-state operating line of near optimal efficiency. Like the

VBV actuators, the VAFN actuators are open-loop scheduled based on corrected fan speed, denoted as N_{1c} for the turbofans and N_{tc} for the tailfan.

3.2.3 Thrust Schedules. Using the STARC-ABL NPSS model, thrust schedules are constructed for the turbofan and tailfan as three-dimensional interpolation grids spanning altitude, Mach, and PLA settings. These schedules produce the target thrust feedback parameter used by the closed-loop controllers of the turbofans and tailfan. In this study, corrected fan speeds $(N_{1c}$ and $N_{tc})$ are chosen as the feedback parameter, which is commonly used as a proxy for thrust in aircraft engine control design [27]. Under most operating conditions, the thrust schedules result in the generators extracting approximately 28% of the total power delivered to the LP shaft of each turbofan by its low-pressure turbine. This level of power extraction allows the steady-state operating line of the turbofans to reside near a region of peak efficiency, particularly when operating at cruise conditions. The 28% power extraction level is maintained at all operating conditions where the tailfan motor remains below its maximum 3500hp limit. However, at most flight conditions higher PLA thrust demands will result in the tailfan reaching the 3500hp limit, which will limit the tailfan speed and thrust output. Under such conditions, increasing PLA beyond the point where the motor limit is encountered will cause an increase in turbofan speed and thrust output while the tailfan motor speed and thrust remains "plateaued" at the limit. The power extraction ratio will also drop below 28% at PLA settings above which the tailfan motor limit is encountered.

3.3 Integrated Control of Subsystems

The schedules discussed in Section 3.2 perform suitably well in ensuring efficient operation of the STARC-ABL under steady-state conditions. However, during transients the turbofan and tailfan subsystems must be operated in a coordinated fashion given the coupling between tailfan power demand and turbofan power extraction induced by the action of the bus voltage controller. Too much power extraction can lead to HPC stall during acceleration, while too little power extraction can cause LPC stall during deceleration. A simple notional example of uncoordinated turbofan and tailfan operation is shown in Fig 3a. Here, it is assumed that the turbofans and tailfan are independently controlled by separate controllers each receiving PLA burst/chop command inputs. Shown are normalized fan speed transient responses for the turbofans and the tailfan. It is possible to design separate turbofan and tailfan controllers that result in the subsystems exhibiting similar speed response during the initial portion of the acceleration transient followed by the turbofans continuing to accelerate after the tailfan plateaus at its maximum motor power limit. However, a potential problem arises on the abrupt PLA chop. Here, the tailfan begins the deceleration with a "head start" due to its lower plateauing speed starting point. This allows the tailfan to lead the turbofans during the deceleration presenting a potential turbofan LPC stall concern. The solution applied to address this transient mismatch concern is to first assume that a single PLA throttle input is used to control operation of the entire STARC-ABL propulsion

system. The single PLA input is used to lookup a target N_{1c} command $(N_{1c,cmd})$ that is provided to both turbofan controllers while an additional "synthesized" PLA command is calculated and provided to the tailfan controller. This tailfan "synthesized" PLA is implemented as a three-dimensional interpolation grid based on altitude, Mach, and the average N_{1c} speed of the two turbofans. The tailfan synthesized PLA will promote more synchronized operation of the turbofans and tailfan during transients as notionally illustrated in Fig 3b. It also allows the integrated control design to be formulated as a SISO control problem as shown in Fig. 4 and discussed in subsection 3.4.

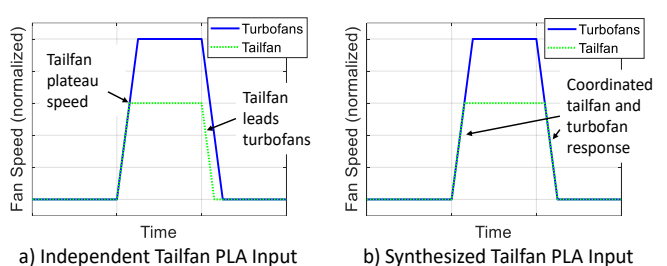


Figure 3: NOTIONAL ILLUSTRATION OF TURBOFAN AND TAILFAN TRANSIENT OPERATION

3.4 Setpoint Control Design

The STARC-ABL integrated control architecture shown in Fig. 4 transforms the turbofan control design into a SISO control problem ($N_{1c,cmd}$ input to N_{1c} output) that captures the subsystem coupling inherent in the system. This formulation readily lends itself to linear control design techniques. The linear state-space model applied for control design is of the following form reflecting deviations (Δ 's) about a trim condition:

$$\Delta \dot{x} = A \Delta x + B \Delta u$$

$$\Delta y = C \Delta x$$
(1)

with deviations in the state variable vector, Δx , the control input vector, Δu , and the sensed measurement vector, Δy . Throughout the remainder of this paper the Δ terms are dropped for simplification. For control design purposes, only one turbofan and the tailfan are considered within the state space model. This simplification is possible due to the symmetric operating nature of the two turbofans. The resulting parameters of the linear state space model are shown in Table 1. They include three states, two outputs, and two inputs. Linearization of the nonlinear STARC-ABL model yields the linear state space system shown in Eq. (2).

Table 1. LINEAR STATE SPACE MODEL PARAMETERS

State Variables (x)	N_{2c}	Turbofan corrected LP shaft speed
	N_{3c}	Turbofan corrected core speed
	N_{tc}	Tailfan corrected speed
Outputs (y)	N_{1c}	Turbofan corrected fan speed
	N_{tc}	Tailfan corrected speed
Inputs (u)	W_f	Turbofan fuel flow
	Q_m	Tailfan motor torque

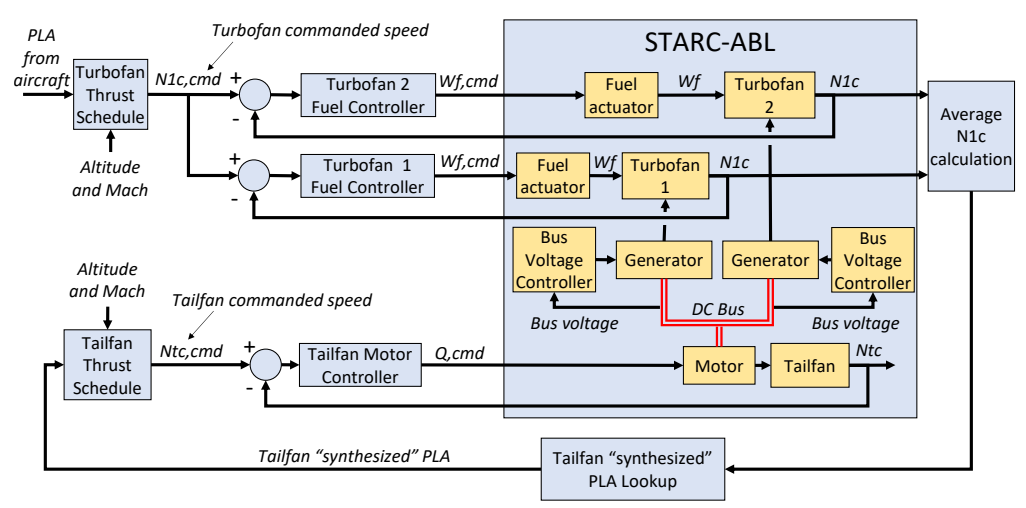


Figure 4: STARC-ABL INTEGRATED CONTROL ARCHITECTURE

$$\frac{\begin{bmatrix} N_{2c} \\ \dot{N}_{3c} \\ \dot{N}_{tc} \end{bmatrix}}{\dot{x}} = \underbrace{\begin{bmatrix} A_{11} & A_{12} & 0 \\ A_{21} & A_{22} & 0 \\ 0 & 0 & A_{33} \end{bmatrix}}_{A} \underbrace{\begin{bmatrix} N_{2c} \\ N_{3c} \\ N_{tc} \end{bmatrix}}_{x} + \underbrace{\begin{bmatrix} B_{11} & B_{12} \\ B_{21} & 0 \\ 0 & B_{32} \end{bmatrix}}_{B} \underbrace{\begin{bmatrix} W_f \\ Q_m \end{bmatrix}}_{u}$$

$$\underbrace{\begin{bmatrix} N_{1c} \\ N_{tc} \end{bmatrix}}_{y} = \underbrace{\begin{bmatrix} C_{11} & 0 & 0 \\ 0 & 0 & 1 \end{bmatrix}}_{c} \underbrace{\begin{bmatrix} N_{2c} \\ N_{3c} \\ N_{tc} \end{bmatrix}}_{x}$$
(2)

Based on the zero entries in the A and B matrices we can see that there is limited coupling between the turbofan and tailfan subsystems. Changes in any individual subsystem state will not affect the state(s) in the other subsystem, and changes in the turbofan fuel flow input will not affect the tailfan state. One parameter that does result in cross-subsystem coupling is the tailfan motor torque input reflected in the second column of the B matrix. Changes to the motor torque input will not only affect tailfan motor speed (as reflected in B_{32}) but will also affect the turbofan LP shaft speed as highlighted in B_{12} term. This is a coupling occurring through the STARC-ABL electrical system as any change in tail motor torque will result in a corresponding change in the amount of generator torque extracted from the turbofan LP shaft to produce the electrical power required to hold the bus voltage constant. Due to system nonlinearities, the A and B matrix entries will vary with operating condition changes in altitude, Mach number, and fan speed. Conversely, the elements of the C matrix are constant and do not change with varying operating condition. The C_{11} term is 0.37037, which is the inverse of the gear ratio between the geared turbofan's LP shaft and fan shaft.

Given this setup, the STARC-ABL closed-loop control architecture can be redrawn in block diagram form as illustrated in Fig. 5. Here, the turbofan detail is expanded to show integrator blocks and state space matrix elements from Eq. (2). Transfer functions reflecting dynamics of the fuel actuator and the tailfan are denoted as F(s) and $G_t(s)$, respectively. Sensor dynamics as well as motor and generator actuator dynamics are excluded

from the figure and the control design process as they are assumed to occur on a time scale considerably faster than the turbofan and tailfan shaft dynamics. Also excluded are VBV and VAFN dynamics as they are assumed to operate on-schedule. The setpoint control design process requires design of the two proportional plus integral (PI) controllers, denoted as K(s) for the turbofan fuel controller and $K_m(s)$ for the tailfan motor controller. The gain block, γ , reflects the fractional change in commanded tailfan corrected speed, $N_{tc,cmd}$, based on a change in turbofan corrected fan speed, N_{1c} , which is consistent with the choice of constructing a synthesized tailfan PLA based on the average N_{1c} of the two turbofans. This N_{tc} : N_{1c} ratio can be thought of as the small perturbation relationship between turbofan and tailfan speeds at a given design point. Consistent with Eq. (2), Motor torque, $Q_m(s)$, is shown as an input feeding directly into both the tailfan and the turbofan.

The tailfan transfer function $G_t(s)$ takes the form of a single spool propulsor with gain K_t and pole r_t . For the STARC-ABL, the values of K_t and r_t are the linear state space model element B_{32} and $-A_{33}$, respectively, as shown in Eq. (3)

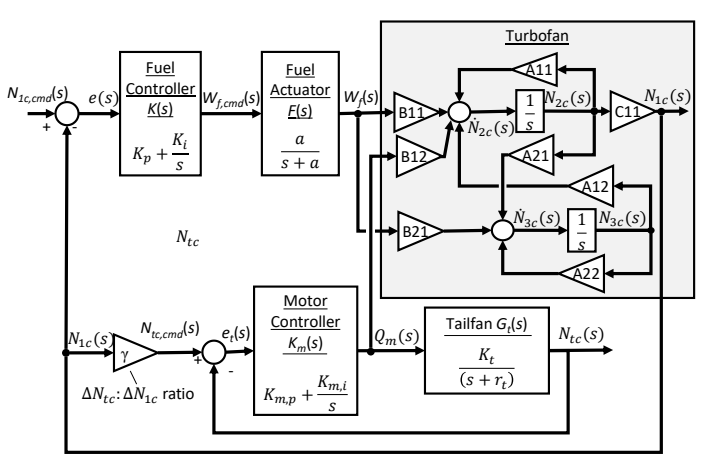


FIGURE 5: STARC-ABL CLOSED-LOOP CONTROL ARCHITECTURE

$$G_t(s) = \frac{K_t}{(s+r_t)} = \frac{B_{32}}{(s-A_{33})}$$
 (3)

Open-loop and closed-loop tailfan transfer functions can be constructed as shown in Eq. (4) and Eq. (5), respectively.

$$OLTF_{tail} = \frac{N_{tc}(s)}{e_t(s)} = K_m(s)G_t(s)$$

$$= \frac{K_{m,p}K_t\left(s + \frac{K_{m,i}}{K_{m,p}}\right)}{s(s + r_t)}$$
(4)

$$CLTF_{tail} = \frac{N_{tc}(s)}{N_{tc,cmd}(s)} = \frac{K_{m}(s)G_{t}(s)}{I + K_{m}(s)G_{t}(s)}$$

$$= \frac{K_{m,p}K_{t}\left(s + \frac{K_{m,i}}{K_{m,p}}\right)}{s(s + r_{t}) + K_{m,p}K_{t}\left(s + \frac{K_{m,i}}{K_{m,p}}\right)}$$
(5)

Also defined is the loop transfer function, T(s), shown in Eq. (6). T(s) relates $N_{tc,cmd}$ to $Q_m(s)$ and will be used to capture the relationship between motor power delivered to the tailfan and the amount of LP shaft power extracted from each turbofan:

$$T(s) = \frac{Q_m(s)}{N_{tc,cmd}(s)} = \frac{K_m(s)}{I + K_m(s)G_t(s)}$$

$$= \frac{K_{m,p}\left(s + \frac{K_{m,i}}{K_{m,p}}\right)(s + r_t)}{s(s + r_t) + K_{m,p}K_t\left(s + \frac{K_{m,i}}{K_{m,p}}\right)}$$
(6)

From Fig. 5, an open-loop transfer function relating turbofan W_f input to N_{1c} output can be written as

$$\frac{N_{1c}(s)}{W_f(s)} = \frac{B_{11}C_{11}\left(s + \frac{A_{12}B_{21}}{B_{11}} - A_{22}\right)}{(s - A_{11})(s - A_{22}) - A_{12}A_{21} - C_{11}\gamma T(s)B_{12}(s - A_{22})}$$

$$= \frac{B_{11}C_{11}\left(s + \frac{A_{12}B_{21}}{B_{11}} - A_{22}\right)}{s^2 - (A_{11} + A_{22})s + (A_{11}A_{22} - A_{12}A_{21}) - C_{11}\gamma T(s)B_{12}(s - A_{22})}$$

Tailfan power extraction coupling effects are captured in the $C_{11}\gamma T(s)B_{12}(s-A_{22})$ portion of the Eq. (7) denominator. The numerator and the remaining portion of the denominator take the following form of a two-spool turbofan engine without power extraction [27]

$$\frac{N_{1c}(s)}{W_f(s)} = \frac{K_e(s+z_1)}{(s+r_1)(s+r_2)} \tag{8}$$

Applying the quadratic formula to calculate roots r_1 and r_2 , and defining the transfer function gain as $K_e = B_{11}C_{11}$ and the zero as $z_1 = \frac{A_{12}B_{21}}{B_{11}} - A_{22}$ allows Eq. (7) to be rewritten as

$$\frac{N_{1c}(s)}{W_f(s)} = \frac{K_e(s+z_1)}{[(s+r_1)(s+r_2) - C_{11}\gamma T(s)B_{12}(s-A_{22})]}$$
(9)

At operating points where the tailfan motor is operating at its maximum hp limit, the γ term becomes zero and Eq. (9) reduces to Eq. (8).

Adding dynamics of the fuel controller and fuel actuator to Eq. (9) yields the following turbofan open-loop transfer function

$$OLTF_{turbofan} = \frac{N_{1c}(s)}{e(s)}$$

$$= \frac{K_p\left(s + \frac{K_i}{K_p}\right) a K_e(s + z_1)}{s(s + a)[(s + r_1)(s + r_2) - C_{11}\gamma T(s)B_{12}(s - A_{22})]}$$
(10)

And the turbofan closed-loop transfer function becomes

$$CLTF_{turbofan} = \frac{N_{1c}(s)}{N_{1c,cmd}(s)} = \frac{OLTF_{turbofan}}{I + OLTF_{turbofan}}$$
(11)

Multiplying Eqs. (5) and (11) also allows the construction of the following transfer function relating $N_{1c,cmd}$ input to N_{tc} output.

$$\frac{N_{tc}(s)}{N_{1c,cmd}(s)} = \frac{N_{tc}(s)}{\underbrace{N_{1c}(s)}_{CLTF_{tail}}} \cdot \underbrace{\frac{N_{1c}(s)}{N_{1c,cmd}(s)}}_{CLTF_{turbofan}}$$

$$= CLTF_{tail} \cdot CLTF_{turbofan}$$
(12)

The setpoint control design process requires selection of the PI control gains for the turbofan fuel controller and the tailfan motor controller. In this study, gain selection is performed in a two-step process with the tailfan motor controller gains, $K_{m,n}$ and $K_{m,i}$, being selected first. This is performed using an optimization routine designed to produce a tailfan closed-loop system (Eq. (5)) meeting user-specified targets for step response rise time and percent overshoot. Due to the integrated control design strategy of calculating a tailfan "synthesized" PLA command based on turbofan N_{1c} speed the tailfan response will necessarily lag that of the turbofans. However, if desired this dynamic lag can be lessened by selecting motor control gains that result in a faster tailfan response. In this study, it was found that selecting rise time and percent overshoot targets matching those of the tailfan open-loop system, Eq. (3), yielded good results. After the tailfan motor controller PI gains are selected the second step of the control design process is the selection of turbofan fuel controller gains, K_n and K_i . This done by first inserting the tailfan controller gains, $K_{m,p}$ and $K_{m,i}$, produced in the first step into Eq. (6) to construct the power extraction transfer function, T(s). Once T(s)

(7)

is obtained, it is inserted into the turbofan closed-loop transfer function given in Eq. (11) and the selection of turbofan PI control gains, K_p and K_i is commenced. This is also performed via an optimization routine that seeks to achieve user-specified targets for step response rise time and percent overshoot for the turbofan closed-loop system.

To illustrate the controller gain selection process, consider the following setpoint control design example for the sea-level-static $N_{1c} = 2600$ rpm operating point. Here, the A, B, and C matrices are given as

$$A = \begin{bmatrix} -1.5226 & 1.5133 & 0\\ 1.9357 & -7.5713 & 0\\ 0 & 0 & -4.6415 \end{bmatrix}$$

$$B = \begin{bmatrix} 1.9308 & -0.24472\\ 6.9348 & 0\\ 0 & 0.39821 \end{bmatrix}$$

$$C = \begin{bmatrix} 0.37037 & 0\\ 0 & 1 \end{bmatrix}$$
(13)

The first step in the control design process produces tailfan PI control gains of $K_{m,p} = 9.78$ and $K_{m,i} = 49.80$. A comparison of the resulting tailfan open-loop and closed-loop step responses is shown in Fig. 6, which illustrates good matching in rise time and percent overshoot as intended for this example.

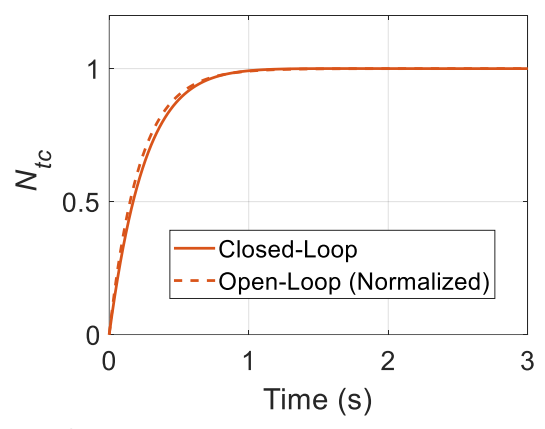


Figure 6: COMPARISON OF TAILFAN OPEN-LOOP AND CLOSED-LOOP STEP RESPONSE

The second step in the control design process selects the turbofan fuel controller PI control gains. In this example we will also select control gains that result in matching rise time and percent overshoot for the turbofan open-loop and closed-loop systems given in Eq. (10) and Eq. (11), respectively. This produces control gains of $K_p = 1.065$ and $K_i = 2.031$. Once PI control gains are chosen, the dynamic closed-loop response of the system can be analyzed using classical linear control design techniques applied to the turbofan and tailfan open-loop and closed-loop transfer functions. This is illustrated in Fig. 7, which shows system step responses, bode plots, and pole-zero maps.

The step response plots show that the turbofan closed-loop (Eq. (11)) and open-loop (Eq. (10)) systems exhibit similar rise time and percent overshoot as intended. It is noted that the tailfan step response shown in Fig. 7, which is based on Eq. (12), has a rise time approximately 2.5 times slower than the tailfan step response shown in Fig. 6 based on Eq. (5). This is due to the dynamic lag inherent in the "synthesized" tailfan PLA command based on turbofan N_{1c} speed. The bode plot information is based on open-loop transfer functions for the turbofan and its controller given in Eq. (10) and the tailfan and its controller given in Eq. (4). The bode plots show that both controllers provide greater than 45 degrees phase margin as recommended by Jaw in Ref [27]. The pole-zero map information shows that the closed-loop turbofan and closed-loop tailfan have identical poles, located at -10.63, -6.12, -4.09 ± 1.56 i, and -1.66 ± 0.47 i. The turbofan has four zeros while the tailfan has three zeros. They share common zeros at -13.01 and -1.91, while the turbofan has a unique complex conjugate pair zeros at -4.27 ± 1.27 , and the tailfan has a unique zero located at -5.0915. If desired, the linear control design analysis methods illustrated in Fig. 7 can be applied to evaluate the effect of adjustments made to the four PI control parameters.

3.5 Transient Controllers and Limit Logic

The set point controllers described in Section 3.4 regulate the STARC-ABL's operation in the presence of minor PLA and operating condition changes. However, during large changes the setpoint controllers alone are not sufficient to ensure compressor operability or the adherence to system operating limits. To address these needs, the control design also includes turbofan transient controllers and control limit logic, which are discussed in Sections 3.5.1 and 3.5.2, respectively.

3.5.1 Turbofan Transient Controllers. Turbofan transient controllers are necessary to ensure that operating limits and adequate turbofan compressor stall margins are maintained during rapid transients. To provide this functionality, PI-based transient controllers are designed to follow defined acceleration and deceleration schedules of corrected fan speed derivative, \dot{N}_{1c} , versus corrected fan speed, N_{1c} , spanning the flight envelope. Selecting \dot{N}_{1c} as the transient control parameter is advantageous as it allows both turbofans to accelerate and decelerate at a similar rate even in the presence of slight performance mismatches between the two engines. The acceleration schedules are designed to accelerate the system from idle to 95% of maximum thrust in under 5 seconds while adhering to a constraint that the turbofan HPC stall margin be no less than 10% during any portion of the transient. At lower altitude and Mach conditions defining acceleration schedules to meet the 5s response time is readily achievable while at higher altitudes and Mach conditions the acceleration schedules exceeding 5s are necessary to meet the 10% HPC stall margin constraint. Deceleration schedules are designed to maintain a minimum LPC stall margin of approximately 5%.

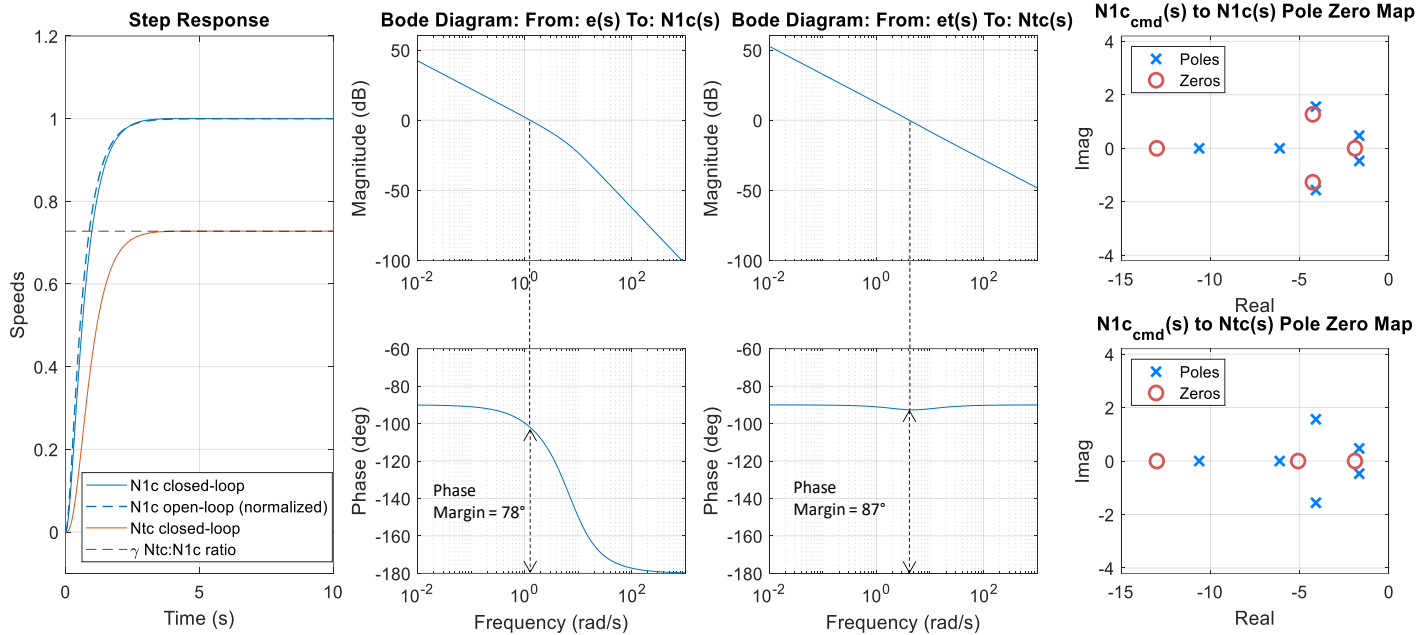


FIGURE 7: INTEGRATED SYSTEM STEP RESPONSES, BODE DIAGRAMS, AND POLE ZERO MAPS

Transient controller development leverages the relationship $\dot{N}_{1c} = s \cdot N_{1c}$, which allows a linear open-loop control transfer function relating e(s) input to $\dot{N}_{1c}(s)$ output to be obtained by multiplying the numerator of Eq. (10) by s as shown in Eq. (14)

$$\frac{\dot{N}_{1c}(s)}{e(s)} = \frac{s \cdot N_{1c}(s)}{e(s)} = s \cdot OLTF_{turbofan}$$
 (14)

Given Eq. (14), a closed-loop transfer function relating $\dot{N}_{1c,cmd}$ input to \dot{N}_{1c} output can be created as shown in Eq. (15)

$$\frac{\dot{N}_{1c}(s)}{\dot{N}_{1c,cmd}(s)} = \frac{s \cdot OLTF_{turbofan}}{I + s \cdot OLTF_{turbofan}}$$
(15)

Given Eq. (15), transient controller PI gains are selected applying linear control design techniques as described for the set point controllers in Section 3.4. It is noted that transient control schedules are only included in the turbofan controller and are not included in the tailfan controller. This simplification is possible due to the natural lagged response in the tailfan synthesized PLA.

3.5.2 Control Limit Logic. In addition to the setpoint and transient control schedules, two control limits are also included in the control design. This includes a tailfan motor maximum power limit and a turbofan minimum HPC exit static pressure, P_{s3} , limit. The motor maximum power limit is a fixed limit set at 3500hp while the minimum P_{s3} limit is a variable limit set to 99% of the idle trim value of P_{s3} at each flight condition. Inclusion of the minimum P_{s3} limit helped maintain LPC stall margin during decelerations. This minimum P_{s3} limit controller is designed as a PI fuel controller using P_{s3} as the feedback parameter.

3.6 Control Integration and Mode Selection Logic

System-level control system design is performed by designing linear setpoint, transient, and limit controllers at multiple operating points spanning the STARC-ABL operating envelope. The resulting linear controllers are then combined in a piecewise linear gain scheduling fashion to provide nonlinear full operating envelope control functionality [27]. Throughout a flight, the control system automatically switches its operating mode between setpoint, transient, and limit controllers by applying conventional maximum-minimum (max/min) mode selection logic to select which control regulator is active at any instant in time [27,28]. Transition between the controllers is managed by integrator windup protection-based bumpless transfer logic as described in Ref. [29]. The max/min control selection logic is illustrated in Fig. 8, showing the setup for the turbofan and tailfan controllers.

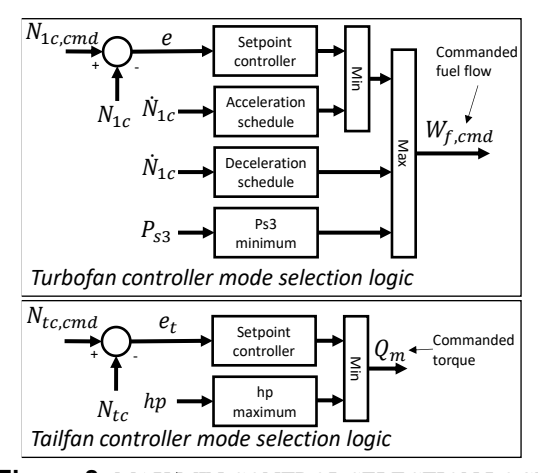


Figure 8: MAX/MIN CONTROL SELECTION LOGIC

Simulated results illustrating system performance with the integrated control design during PLA burst/chop transients at sea level static and a cruise condition of 39K feet Mach 0.785 are shown in Fig. 9 and Fig. 10, respectively. Here, the single PLA command provided to the turbofans transitions from idle to maximum at time 10s and from maximum to idle PLA at time 30s. The synthesized tailfan PLA, as expected, exhibits a lag relative to the turbofan PLA as it is based on sensed turbofan N_{1c} .

At sea level static conditions, the acceleration transient occurs in less than 5s and the deceleration transient requires approximately 10s. Here, HPC stall margin is observed to reduce during the acceleration transient reaching a minimum of approximately 17%. LPC stall margin reaches a minimum of approximately 8% during the deceleration portion of the transient. The control mode selection plots illustrate how the turbofan controller transitions operation between the setpoint controller, the acceleration and deceleration transient controllers, and the minimum Ps3 controller during the transient. The tailfan controller operates under setpoint control for most of the run but does briefly encounter the maximum motor horsepower limit during the acceleration portion of the transient.

The cruise acceleration and deceleration transients occur more slowly than at sea level static, with the acceleration requiring approximately 10s and the deceleration approximately 20s. Here, the acceleration transient control schedule is defined to maintain the desired HPC minimum stall limit of 10% which is encountered near 17s. During the deceleration transient the deceleration transient control schedule is first activated followed by the minimum P_{s3} control limiters. Collectively this results in a minimum LPC stall margin of approximately 5% encountered near 37s. Less motor power is required to drive the tailfan at cruise and the tailfan maximum hp limit is not encountered.

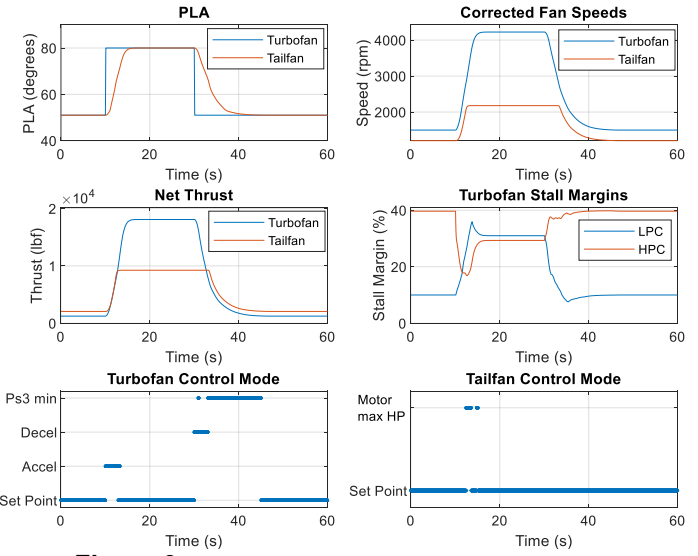


Figure 9: SEA LEVEL STATIC PLA BURST CHOP

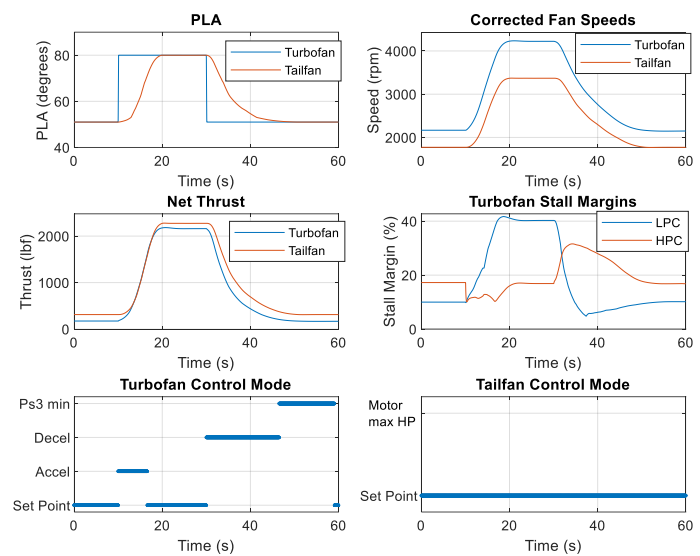


Figure 10: CRUISE (39K FEET, 0.785 MACH) PLA BURST CHOP

4.1 Test Configuration

The NEAT STARC-ABL controls test was configured as a partially simulated, partially hardware-in-the-loop experiment as shown in Fig. 11. Here, a full-scale nonlinear simulation of the turbofan and tailfan turbomachinery and the control software are implemented in a real-time computer (shown in the top half of Fig. 11) while a subscale version of the STARC-ABL electrical system and associated turbofan LP shaft and tailfan shaft dynamics are implemented in actual hardware (shown in the bottom half of Fig. 11). The hardware configuration includes eight 250kW electric machines each equipped with an inverter configured to accept torque command inputs and supply speed feedback measurements. The electric machines are mechanically coupled to emulate three separate rotating shafts: Turbofan1, Turbofan 2, and the Tailfan. Two of the shafts consist of electric machine pairs where one machine emulates turbofan LP shaft dynamics while the second operates as a turbofan generator. The third shaft consists of four electric machines, where two of the machines operate in tandem to emulate tailfan shaft dynamics and the remaining two machines operate in tandem to represent the tailfan motor. The hardware configuration also includes two 700V DC power buses, both supplied by unidirectional DC power supplies. Electric machines representing the STARC-ABL motor and generators are connected to the research bus while electric machines used to emulate turbofan LP and tailfan shaft dynamics are connected to the emulation bus. While not part of the actual STARC-ABL concept, adjustable load banks are included on each bus of the NEAT configuration. Their inclusion is a precautionary measure to guard against potential reverse power flow events, which could damage the electrical hardware. The subscale electrical system operates at approximately 10% of the full-scale STARC-ABL power level.

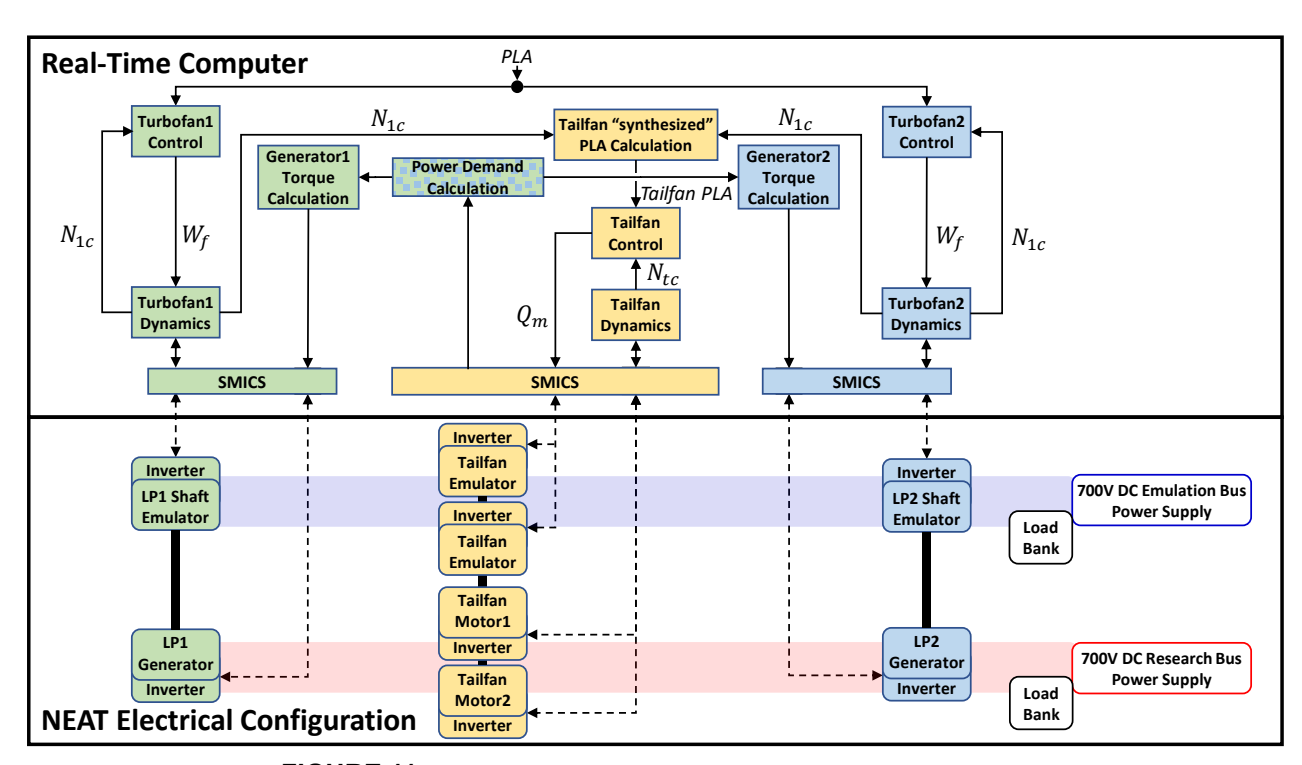


FIGURE 11: NEAT STARC-ABL CONTROLS TEST CONFIGURATION

To allow the STARC-ABL integrated control design to be tested at NEAT without modification several differences between the full-scale STARC-ABL and subscale NEAT electrical systems are accounted for. This includes differences in electric machine power levels, rated operating speeds, rotational shaft inertia, and viscous damping. To address these inconsistencies, an innovative sliding mode impedance controller with scaling (SMICS) approach is applied to scale the torque and speed signals passed between the real-time computer and the electrical hardware and to allow the electric machines tasked with emulating turbomachinery shaft dynamics to accurately emulate the desired inertias and loads [30]. Also, the efficiencies of the subscale NEAT electric machine and inverter hardware do not match the full-scale STARC-ABL electrical system efficiencies that the control system is designed for. This requires the inclusion of the software-based "power demand calculation" block shown in the top half of Fig. 11. This calculation produces a scaled torque command supplied to the generators based on the electrical power demand of the tailfan motor. This implements the coupling between the tailfan and the turbofans in the NEAT configuration.

4.2 NEAT Test Results

The NEAT test campaign evaluated the STARC-ABL integrated control design under a variety of transient operating scenarios. This included PLA throttle transients introduced at simulated altitude and Mach conditions spanning the STARC-ABL's flight envelope. Throttle transient results from the 20K feet, 0.6 Mach flight condition are shown in Fig. 12. Simulation inputs are shown in the top row of the figure and include the

static altitude and Mach inputs plus the turbofan PLA throttle transient profile. This 6-minute profile includes up and down ramps, up and down stairsteps, and a burst and chop ranging from idle to maximum PLA. The remaining figure subplots show shaft speed, stall margin, net thrust, fuel flow, and electric machine torque data acquired during the test. The speed and torque data shown are full-scale (i.e., unscaled) versions of the actual speed and torque data acquired from the NEAT research bus electrical machine hardware during the test while the stall margin, net thrust, and full flow data is from the real-time simulation. For each parameter the NEAT experimental results are plotted against pre-test simulation prediction results of the same parameter. The experimental and simulation results exhibit good agreement with less than 1% mean absolute error in all parameters. This includes the turbofan LP shaft speed, tailfan speed, generator torque, and motor torque parameters which are direct scaled versions of the speeds and torques of the NEAT electric machine hardware.

In addition to the throttle profile tests, the NEAT test campaign also included several mission profile tests that subjected the STARC-ABL integrated control design to realistic full-flight altitude, Mach, and PLA variations. Example results based on actual flight data obtained from the NASA Ames DASHLink website [31] are shown in Fig. 13. This 70-minute full-flight profile subjected the integrated control design to taxi, takeoff, climb, cruise, decent, and landing flight phases. Once again, the control system performed as intended. No operability issues were encountered and experimental results are found to match pre-test simulation predictions within 1% accuracy.

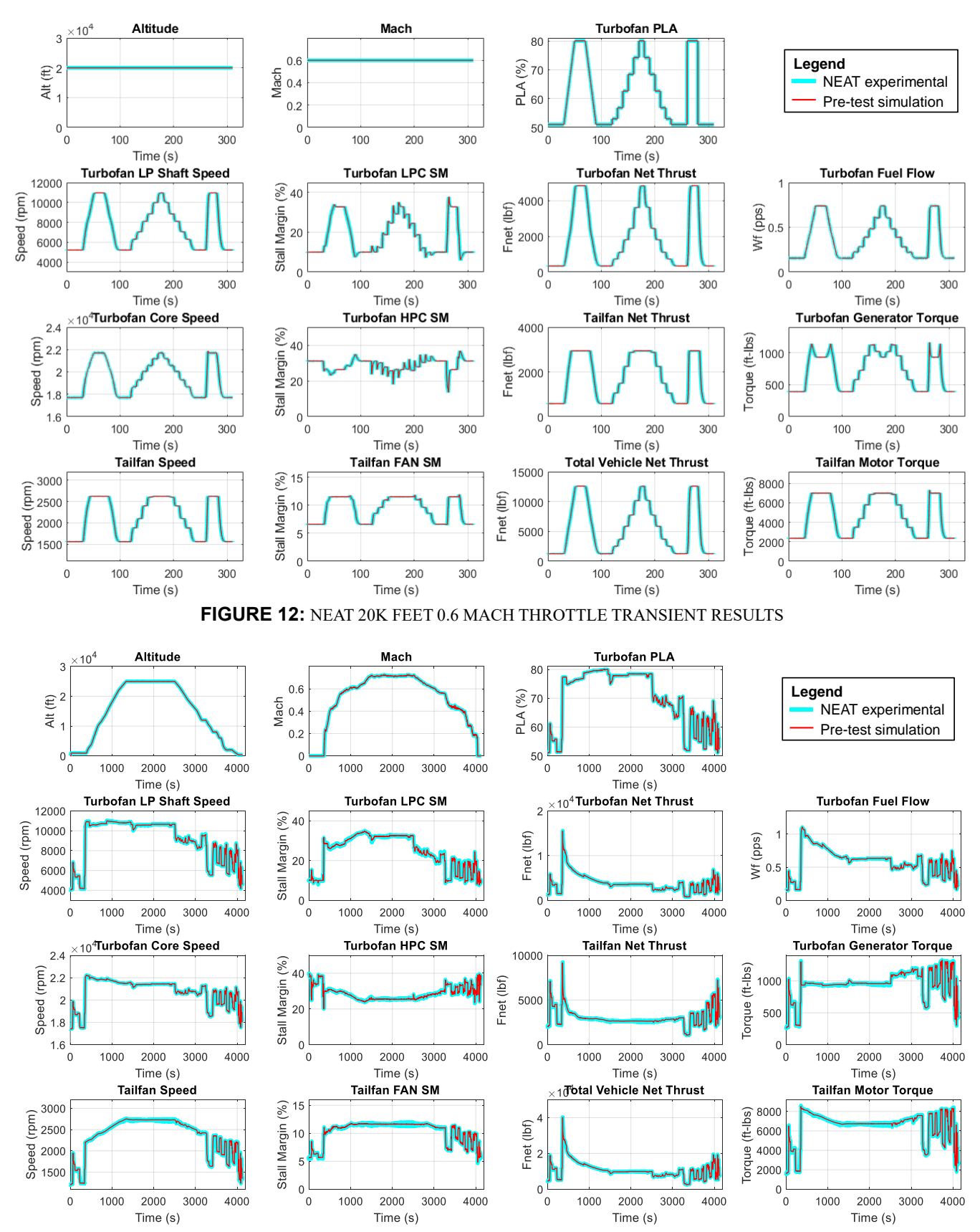


FIGURE 13: NEAT ACTUAL MISSION PROFILE RESULTS

The NEAT STARC-ABL controls evaluation included over 140 individual throttle transient and mission profile tests and collected approximately 15 hours of test data. In addition to executing the throttle profile and mission profile test cards under nominal (undegraded) health conditions these same test cards were also executed under 50% (midlife) and 100% (end-of-life) simulated degradation conditions to assess the robustness of the control design. In all cases the integrated control design maintained the operability of the overall system, demonstrating its robustness to these representative variations. A detailed description of the NEAT STARC-ABL controls test configuration and test results is provided in Ref. [32].

4. DISCUSSION

The presented integrated control design strategy relies on derived loop transfer functions that reflect the coupling the subsystems of an EAP architecture. Although this paper has only demonstrated the approach against the STARC-ABL concept, the same strategy has applicability to any EAP architecture exhibiting such coupling between subsystems. Requirements for applying this strategy are to have a control concept of operations that defines the coordinated operation of subsystems and a system model suitable for control design purposes. Follow on work is recommended to evaluate integrated control strategies for additional EAP concept architectures.

Due to the coupled nature of EAP architectures, follow-on work is also recommended to assess the impact of subsystem failures and the potential need to reconfigure system-level control logic in the presence of such events. Initial work in this area for the STARC-ABL was presented in Ref. [33] applying a decentralized approach towards the control design. However,

REFERENCES

- [1] Jansen, R.H., Bowman, C., Jankovsky, A., Dyson, R., Felder, J., (2017), "Overview of NASA Electrified Aircraft Propulsion Research for Large Subsonic Transports," AIAA-2017-4701, AIAA Propulsion and Energy Forum, Atlanta, GA, July 10-12.
- [2] Felder, J.L., (2015), "NASA Electric Propulsion System Studies," presentation, 5th EnergyTech 2015, Cleveland, OH, Nov. 30 Dec 2.
- [3] National Academies of Sciences, Engineering, and Medicine. 2016. Commercial Aircraft Propulsion and Energy Systems Research: Reducing Global Carbon Emissions. Washington, DC: The National Academies Press. https://doi.org/10.17226/23490.
- [4] Schäfer, A. W., Barrett, S. R., Doyme, K., Dray, L. M., Gnadt, A. R., Self, R., Torija, A. J. (2019), "Technological, Economic and Environmental Prospects of All-Electric Aircraft," *Nature Energy*, 4(2), 160-166.
- [5] Jansen, R., Brown, G.V., Felder, J.L., and Duffy, K.P., (2015), "Turboelectric Aircraft Drive Key Performance Parameters and Functional Requirements," AIAA 2015-3890, AIAA Propulsion and Energy, Orlando, Florida, July 27–29.

follow-on work is recommended applying the new integrated control design strategy presented in this paper.

5. CONCLUSIONS

An integrated control strategy for maintaining coordinated transient operation of electrified aircraft propulsion architecture subsystems has been presented. The approach is applied to a distributed partially-turboelectric propulsion architecture consisting of two turbofan engines that produce thrust and supply mechanical offtake power for the generation of electricity supplied to a motor driven tailfan propulsor. Operation of the tailfan is scheduled as a function of turbofan fan speed, which allows the construction of linear loop transfer functions capturing the open- and closed-loop dynamic response of the system. This enables the turbofan control design problem to be transformed into a single-input-single-output problem that readily lends itself to classical linear control design and analysis techniques. Piecewise linear setpoint controllers, transient control schedules, and limit controllers are developed and integrated to produce a full flight envelope integrated control design. A real-time partial hardware-in-the-loop test of the integrated control design demonstrated robust transient system operation in the presence of realistic system input variations.

ACKNOWLEDGEMENTS

This work was conducted under the NASA Advanced Air Vehicles Program, Advanced Air Transport Technology Project, Power and Propulsion Subproject. The authors graciously acknowledge the tremendous support provided by the NEAT facility engineers and technicians that made this research effort possible.

- [6] Friedrich, C., and Robertson, P. A. (2015), "Hybrid-Electric Propulsion for Aircraft," *Journal of Aircraft*, 52(1), 176-189.
- [7] Aeronautics, NASA. (2019), "NASA Aeronautics Strategic Implementation Plan: 2019 Update," Technical Report NP-2017-01-2352-HQ.
- [8] National Aeronautics and Space Administration, (2022), "Sustainable Flight National Partnership," https://www.nasa.gov/aeroresearch/sustainable-aviation-np/
- [9] United States Federal Aviation Authority, (2021), "Aviation Climate Action Plan," United States Federal Aviation Authority, accessed Sept. 23, 2022, https://www.faa.gov/sites/faa.gov/files/2021-11/Aviation Climate Action Plan.pdf
- [10] Zhang, X., Bowman, C. L., O'Connell, T.C., and Haran, K. S., (2018), "Large Electric Machines for Aircraft Electric Propulsion," *IET Electric Power Applications*, 12(6), 767-779
- [11] Cotton, I., Gardner, R., Schweickart, D., Grosean, D., and Severns, C., (2016), "Design Considerations for Higher Electrical Power System Voltages in Aerospace Vehicles,"

- IEEE International Power Modulator and High Voltage Conference (IPMHVC), 57-61.
- [12] Chapman, J. W., Hasseeb, H., and Schnulo, S. (2020), "Thermal Management System Design for Electrified Aircraft Propulsion Concepts" AIAA/IEEE Electric Aircraft Technologies Symposium (EATS) (pp. 1-23).
- [13] Simon, D. L., Connolly, J. W., & Culley, D. E. (2020), "Control Technology Needs for Electrified Aircraft Propulsion Systems," ASME Journal of Engineering for Gas Turbines and Power, 142(1).
- [14] Simon, D. L. (2022), "System-Level Control Concepts for Electrified Aircraft Propulsion Systems," NASA Technical Memorandum TM-20210026284.
- [15] Kratz, J. L., Culley, D. E., and Thomas, G. L., (2019), "A Control Strategy for Turbine Electrified Energy Management," AIAA–2019–4499 AIAA/IEEE Electric Aircraft Technologies Symposium (EATS), Indianapolis, Indiana, August 22–24.
- [16] Misley, A., D'Arpino, M., Ramesh, P., and Canova, M. (2021), "A Real-Time Energy Management Strategy for Hybrid Electric Aircraft Propulsion Systems," AIAA-2021-3283, AIAA/IEEE Electric Aircraft Technologies Symposium (EATS), Virtual, August 9-11.
- [17] Richter, H., Connolly, J.W., and Simon, D.L., (2020), "Optimal Control and Energy Management for Hybrid Gas-Electric Propulsion," *Journal of Engineering for Gas Turbines and Power*, 142(9).
- [18] Doff-Sotta, M., Cannon, M., and Bacic, M., (2023), "Predictive Energy Management for Hybrid Electric Aircraft Propulsion Systems," *IEEE Transactions on Control Systems Technology*, 31(2), 602-614.
- [19] Connolly, J. W., Chapman, J. W., Stalcup, E. J., Hunker, K. R., Chicatelli, A. K., and Thomas, G. L., (2018), "Modeling and Control Design for a Turboelectric Single Aisle Aircraft Propulsion System," AIAA-2018-5010, AIAA/IEEE Electric Aircraft Technologies Symposium (EATS), Cincinnati, Ohio, July 9-11.
- [20] Connolly, J., and Stalcup, E., (2017), "Dynamic Modeling, Controls, and Testing for Electrified Aircraft," In Energy Technology (EnergyTech) Conference, Cleveland, Ohio, October 31.
- [21] Kratz, J.L, Thomas, G.L., (2019), "Dynamic Analysis of the STARC-ABL Propulsion System," AIAA-2019-4182, AIAA Propulsion and Energy Forum, Indianapolis, Indiana, August 22-24.
- [22] Welstead, J.R., Felder, J.L., (2016), "Conceptual Design of a Single-Aisle Turboelectric Commercial Transport with Fuselage Boundary Layer Ingestion," AIAA 2016-1027,

- AIAA SciTech Forum, 54th AIAA Aerospace Sciences Meeting, San Diego, CA, January 4-8.
- [23] Felder, J. L., Schnulo, S. L., Tong, M. T., Berton, J. J., Thacker, R. P., Haller, W. J. (2022), "An Updated Assessment of Turboelectric Boundary Layer Ingestion Propulsion Applied to a Single-Aisle Commercial Transport," AIAA SciTech Forum and Exposition, San Diego, CA, January 3-7.
- [24] Lytle, J., Follen, G., Naiman, C., Evans, A., Veres, J., Owen, K., Lopez, I., (2000), "Numerical Propulsion System Simulation (NPSS) 1999 Industry Review," NASA/TM-2000-209795, August.
- [25] Chapman, J.W., Lavelle, T.M., May, R.D., Litt, J.S., Guo, T-H., (2014), "Toolbox for the Modeling and Analysis of Thermodynamic Systems (T-MATS) User's Guide," NASA/TM-2014-216638, January.
- [26] Chapman, J.W., Litt, J.S., (2018), "An Approach for Utilizing Power Flow Modeling for Simulations of Hybrid Electric Propulsion Systems," AIAA-2018-5018, AIAA Propulsion and Energy Forum, Cincinnati, OH, July 9-11.
- [27] Jaw, L., & Mattingly, J., (2009), "Aircraft Engine Controls," New York, NY, USA: American Institute of Aeronautics and Astronautics.
- [28] May, R.D., Garg, S., (2012), "Reducing Conservatism in Aircraft Engine Response Using Conditionally Active Min-Max Limit Regulators," ASME GT2012-70017, ASME Turbo Expo, Copenhagen, Denmark, June 11-15.
- [29] Chapman, J.W., Litt, J.S., (2017), "Control Design for an Advanced Geared Turbofan Engine," AIAA-2017-4820, *AIAA Propulsion and Energy Forum*, Atlanta, GA, 2017.
- [30] Bianco, S.J., Simon, D.L., (2023), "Control and Scaling Approach for the Emulation of Scaled Dynamic Mechanical Loads," AIAA/IEEE Electric Aircraft Technologies Symposium, San Diego, CA, June 12-16.
- [31] DASHlink— Sample Flight Data, (2012), available online: https://c3.nasa.gov/dashlink/resources/664/ (accessed on 12 October 2022).
- [32] Simon, D.L., Bianco, S. J., Horning, M.A., Saus, J.R., Amthor, A.E., Sachs-Wetstone, J.J., (2023), "Real-time Hardware-in-the-Loop Evaluation of a Partially Turboelectric Propulsion Control Design," AIAA/IEEE Electric Aircraft Technologies Symposium (EATS), San Diego, California, June 12-16.
- [33] Simon, D. L., and Connolly, J. W., (2020), "Electrified Aircraft Propulsion Systems: Gas Turbine Control Considerations for the Mitigation of Potential Failure Modes and Hazards," ASME-GT2020-16335, ASME Turbo Expo Conference, Virtual, Online, September 21-25.